Impact of Beam Diameter and Scanning Approach on Point Cloud Quality of Terrestrial Laser Scanning in Forests

Meinrad Abegg ⓘ, Ruedi Boesch ⓘ, Michael E. Schaepman ⓘ, *Senior Member, IEEE*, and Felix Morsdorf ⓘ

Abstract—In recent years, portable laser scanning devices and their applications in the context of forest mensuration have undergone rapid methodological and technological developments. Devices have become smaller, lighter, and more affordable, whereas new data-driven methods and software packages have facilitated the derivation of information from point clouds. Thus, terrestrial laser scanning (TLS) is now well established, and laser–object interactions have been studied using theoretical, modeling, and experimental approaches. The representation of scanned objects in terms of accuracy and completeness is a key factor for successful feature extraction. Still, little is known about the influence of TLS and survey properties on point clouds in complex scattering environments, such as forests. In this study, we investigate the influence of laser beam diameter and signal triggering on the quality of point clouds in forested environments. Based on the Swiss National Forest Inventory data, we simulate the TLS measurements in 684 virtual forest stands using a 3-D content creation suite. We show that small objects lack sufficient representation in the point cloud and they are further negatively influenced by large laser beam diameters, dense stands, and large distances from the scanning device. We provide simulations that make it possible to derive a rationale for decisions regarding the appropriate choice of TLS device and survey configuration for forest inventories.

Index Terms—Forest inventory, occlusion, simulation, stem diameter distribution.

I. INTRODUCTION

FORESTS cover more than 30% of the global land area, serving as a source of livelihood, protecting soil, water, and infrastructure, holding more than 75% of the world's terrestrial biodiversity, and providing a multitude of ecosystem services [1], [2]. Notably, forests play a vital role in carbon

Meinrad Abegg is with Forest Resources and Management Unit, Swiss Federal Institute for Forest, Snow and Landscape Research WSL, CH-8903 Birmensdorf, Switzerland (e-mail: meinrad.abegg@wsl.ch).

Ruedi Boesch is with Land Change Science Unit, Swiss Federal Institute for Forest, Snow and Landscape Research WSL, CH-8903 Birmensdorf, Switzerland.

Michael E. Schaepman and Felix Morsdorf are with Remote Sensing Laboratories, Department of Geography, University of Zurich, CH-8057 Zürich, Switzerland.

storage [3]. To ensure sustainable management of forests, monitoring is crucial. Forest mensuration provides a large toolset to acquire information on forests, from remote sensing to field measurements on systematic grids in the case of forest inventories. Even though remote sensing covers many aspects of forest monitoring, field measurements are still essential, providing data not measurable by remote sensing or serving as ground truth to calibrate remote sensing products such as wall-to-wall maps of forest features (see [4]). However, certain forest features, such as light availability, crown size, forest structure, and tree volume, are nearly impossible to measure with traditional approaches or only at a very high cost. They are based either on models (e.g., tree volume models) or on expert assessments (e.g., forest structure). The fast development of efficient and lightweight close-range remote sensing technologies in recent years, such as terrestrial laser scanning (TLS) and their applications, raises the question of their applicability for forest mensuration, e.g., in forest inventories [5].

New measurements must be evaluated in terms of efficiency, precision, and the quality of the newly acquired forest information. For close-range scanning applications where ground truth is difficult to acquire [6], one established way to evaluate this technology is the use of simulation approaches (see [7]–[10]). Once a simulation environment is established, it is possible to test many configurations in short time frames. A major advantage of simulation is the possibility to conduct sensitivity studies by comparing different configurations of the same object [11]. The simulation environment is merely an abstraction of reality, and consequently, the representativeness of the virtual scene and the implemented LiDAR technology has to be considered carefully.

The application of laser scanning technologies is dependent on many factors, such as laser geometry properties and the interaction of light with the object surface [12]. Adams and Kerstens [13] and Newnham *et al.* [14] pointed to the phenomenon of "mixed pixels" (edge noise), which occur when a pulse emitted by a laser scanner hits more than one object in its path, may leading to false range measurements. Some authors (see [15], [16]) describe different approaches for signal triggering in time-of-flight systems. Newnham *et al.* [14] mentioned "range averaging" in phase shift laser scanners in case of mixed pixel situations. Furthermore, some approaches exist to simulate the characteristics of various laser scanning

technologies (see [12], [17]), but they are mostly focused on airborne laser scanning systems with large beam diameters and full waveform information (time-of-flight systems). The specific peculiarities of terrestrial laser scanners, phase shift, or time-of-flight systems, working with small laser diameters are mostly unknown even though certain information, such as the intensity pattern of the LiDAR reflections, is sometimes known (see [18], [19]). These publications indicate that there is a gap between theory and real implementation in laser scanners regarding details in signal triggering. In addition, producers of terrestrial laser scanners keep the technical details of the implemented LiDAR technology as industrial secrets.

The goal of this study is to use a simulation approach to understand specific effects, e.g., influence of signal triggering, diameter of the laser beam, or size of the scanned object, on the application of TLS in complex environments, such as forests. We hypothesize that depending on certain properties of the LiDAR device, such as the diameter of the laser beam or the signal triggering approach, there are clear limits to the ability of point clouds to contain accurate geometric information on scanned objects.

In order to conduct this simulation study, we analyze the main "mixed pixel" effects of three TLS devices in experiments performed in a laboratory setting with respect to signal triggering, omission of echoes during scanning, and deviation of scan points from object surfaces, integrate these system effects to a laser scanning simulation environment, and conduct a simulation study using different forest stand characteristics by simulating laser scanners with different laser beam diameters and signal triggering approaches (including distance deviation and filtering), ultimately leading to recommendations for suitable TLS objectives and detectable object (tree and branch) sizes.

II. Materials and Methods

A. Simulating Laser Scanning With Blender

Blender [20] is an open-source 3-D content creation suite. It is designed to easily build digital 3-D objects and their light-interaction properties. It usually generates photorealistic images or animations as output. Blender provides a large toolbox to define, manipulate, and store 3-D objects. As in one of our previous studies [21], we used Blender version 2.74 and fully controlled the simulation using python scripts (Version 2.7.13).

BlenSor is an add-on for Blender that allows access to an internal part of Blender and hence provides the basics to simulate various types of range scanners and other optical instruments [22]. It enables an efficient intersection of mathematical vectors (rays) with 3-D objects defined in Blender and returns the range and the incidence angle on the object surface. Similar to Monte Carlo ray-tracing approaches (see [23]–[25]), single rays of light (photons) can be traced on their way through a virtual scene.

If the geometric properties, i.e., the diameter at exit and the divergence, of the laser emitted by a laser scanning system are known, this ray-tracing capability can theoretically be used to simulate any kind of LiDAR sensor. To do so,

TABLE I
BEAM DIAMETERS AND DIVERGENCES OF DIFFERENT DEVICES ACCORDING TO THE $1/e^2$ DEFINITION

Device	Beam diameter at exit [mm]	Beam divergence [mrad]
Leica BLK360	3.80	0.68
FARO Focus³ᴰ 120	4.24	0.27
Riegl VZ-1000	18.00	0.30

multiple photons (light rays) can be sampled within one laser beam cone. Following an assumed distribution of energy (e.g., Gaussian-shaped), the sampling density can be varied within the laser beam. If it is known exactly how a laser scanner uses the backscattered light to trigger one or multiple echoes, an implementation in Blender enables a realistic laser scanning simulation.

B. Analysis of Terrestrial Laser Scanners

1) Tested Devices: We tested three different portable state-of-the-art terrestrial laser scanners with beam properties (beam diameter at exit and beam divergence), as shown in Table I. The Leica BLK360 uses the "time of flight enhanced by waveform digitizing technology" [26]. It triggers one point per laser pulse and offers a field of view of 360° horizontally and 300° vertically. It measures 100 mm in diameter and 165 mm in height, with a weight of 1 kg. It has a range of 0.6–60 m [26]. The FARO Focus³ᴰ 120 is a phase shift system that sends out a modulated laser beam to trigger a single echo per direction. It offers a field of view of 360° horizontally and 305° vertically, leaving only a small spot beneath the scanner uncovered. Various scan parameters can be adjusted, including the angular resolution and the point cloud quality parameters. It measures 240 × 100 × 200 mm, with a weight of 5 kg. It has a range of 0.6–120 m [27]. The Riegl VZ-1000 is a time-of-flight system, with the ability to capture multiple points per laser pulse and options to provide full-wave data. It offers a field of view of 360° horizontally and 100° vertically. The scanner, measuring 200 × 203 × 308 mm and with a weight of 9.8 kg, has a wide range of adjustable settings, including pulse repetition frequency and angular resolution. It has a range of 2.5–1400 m [28].

2) Experimental Laboratory Setup for the Analysis of Mixed Pixel Effects: We evaluated mixed pixel effects that emerge when two separated objects are intersected by one laser beam cone. This enables us to derive models of point triggering functionalities and describe the most important mixed pixel effects of the examined devices. As preparation, we conducted various test scans with different setups of obstacles at different distances to infer a suitable experimental setup. The final experimental setup is listed in Table II. These setups capture the most important noise effects, previously observed in our data.

As shown in Fig. 1, we placed two objects in the field of view of the scanner: one (obstacle 1) closer to the scanner and the other (obstacle 2) farther away. Obstacle 1 has two horizontal edges at the same height: one is a top edge and the other is a bottom edge. Because edge noise in the point
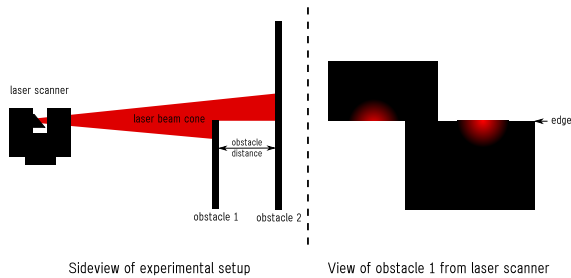
Fig. 1. Setup of lab experiment to analyze edge noise effects of terrestrial laser scanners. Two obstacles are placed at a known distance ("obstacle distance") from each other, in such a way that effects on the point triggering of laser beam cones hitting the two objects can be analyzed. (Left) Side view of the experimental setup when a laser pulse intersects with obstacle 2 and the lower part of obstacle 1. (Right) Footprint of two laser pulses on obstacle 1, both hitting the obstacles with approximately 50% of the beam energy. The laser pulses on the left (and top) part of obstacle 1 are only used to derive the height of the horizontal edge. The laser pulses on the right (and bottom) part are used for both, the derivation of the horizontal edge height and the analysis of the edge noise effects.

TABLE II
SETUP OF THE OBSTACLES FOR THE LAB EXPERIMENTS

Device name	Distance scanner to obstacle 1 [m]	Obstacle distances [m]
Leica BLK360	3.59	0.07, 0.54, 1.95, 3.53, 5.28, 9.53
FARO Focus^{3D} 120	5.01	0.1, 0.2, 0.3, 0.4, 0.5, 0.6, 0.7, 0.8, 0.9, 1.0, 1.1, 1.2, 1.3, 1.4, 1.5, 1.6, 1.7, 1.8, 1.9, 2.0
Riegl VZ-1000	4.91	0.2, 0.4, 0.6, 0.7, 0.8, 0.9, 1.0, 1.1, 1.2, 1.4, 1.6, 1.8, 2.0

cloud at these edges is symmetric, the edge height can be derived from the point cloud directly by comparing the edge noise patterns at the bottom and the top edge. With the known beam diameter at the distance of the obstacle, the amount of laser beam energy hitting the two obstacles can be calculated. The obstacles' surfaces are white sheets of paper with an appropriate thickness to ensure a flat surface.

3) Model Description of Signal Triggering: In this section, we describe the derivation of signal triggering models based on the lab experiments outlined in Section II-B2. Generalized for multiple obstacles, these models can be applied to a simulation study.

As mentioned in Section II-A, the LiDAR simulations, as applied in this study, can only make use of distance measurements to objects with the corresponding energy ratios of simulated laser beam cones hitting them. Hence, the models derived from the lab experiments also rely on these two parameters.

To know which points in the point cloud are based on laser pulses hitting the two objects, the energy ratio of the laser pulse on the two objects was calculated. For this purpose, the size of the laser footprint on the object must be known. Even though only explicitly provided for Riegl [28] and partly for FARO [27], we assumed the laser beam of all three devices

to be circular with a Gaussian-shaped energy distribution. As the three devices use different units to describe the laser beam diameter, we calculated them according to the "1/e²" standard, as described in (1). All the standards provide a means to describe the ratio of the maximally irradiating energy across a laser beam diameter, which is used to define the width between two opposite points where this irradiance ratio is reached

$$D_{B_{(1/e^2)}} = \sqrt{2}D_{B_{(1/e)}} = 1.699 * D_{B_{(FWHM)}} \qquad (1)$$

where $D_{B_{(1/e^2)}}$ is the diameter according to the "1/e²" standard (maximum irradiance/e²), $D_{B_{(1/e)}}$ according to the "1/e" standard (maximum irradiance/e), and $D_{B_{(FWHM)}}$ according to the "full-width at half-maximum (FWHM)" standard (maximum irradiance/2). Assuming a Gaussian-shaped energy distribution, the "1/e²" range within the laser beam contains 95.45% of the energy, covering two times the standard deviation of the Gaussian-distributed energy.

By using a Gaussian distribution function with the expectation value (μ), the standard deviation (σ), and a quantile (q), the energy ratio on the objects can be derived.

a) Leica BLK360: An examination of Leica BLK360 point clouds revealed noise in only very few exceptional cases and no noise at all in the specific setup of the lab experiments. Consequently, we did not derive a noise model. However, as we saw in our analysis (see Fig. 4), the Leica scanner only triggers one echo per laser pulse and does perform a filtering of the point cloud. Because the filtering is executed during the scanning, we refer to it as prefiltering to distinguish it from the filtering of the point cloud as part of processing after the scanning.

For our model derivation, we used laser pulses intersecting the two obstacles with an energy ratio slightly above twice the standard deviation of the energy distribution (from 2% to 98% of the laser beam energy on the two obstacles). A prefiltering model is represented by the probability that an echo (or signal) is triggered (referred to here as "signal triggering probability"). Thus, we derived a model for the signal triggering probability based on the Leica scanner lab data. To obtain the true value of the signal triggering probability, we built equal bins of vertical scan angles and counted the number of points in each bin. An approximation of the triggering probability equals the ratio of the point number per bin to the mean point number in bins without prefiltering. To derive a suitable model for the triggering probability, we only need to analyze the energy ratios $\geq 50\%$ because if the energy ratio of the laser pulse on one of the two obstacles is lower, the point is triggered on the other object (or not at all).

The basis for the signal triggering probability model is a logit function in the following equation:

$$p = \frac{1}{1 + e^{-L}} \qquad (2)$$

where p is the triggering probability and L is a function of the energy ratio of the laser on an obstacle.

The model was fit empirically in the following form, where E_l is the ratio of energy of the laser pulse on the object that obtains the most energy, D_o is the positive distance in meters
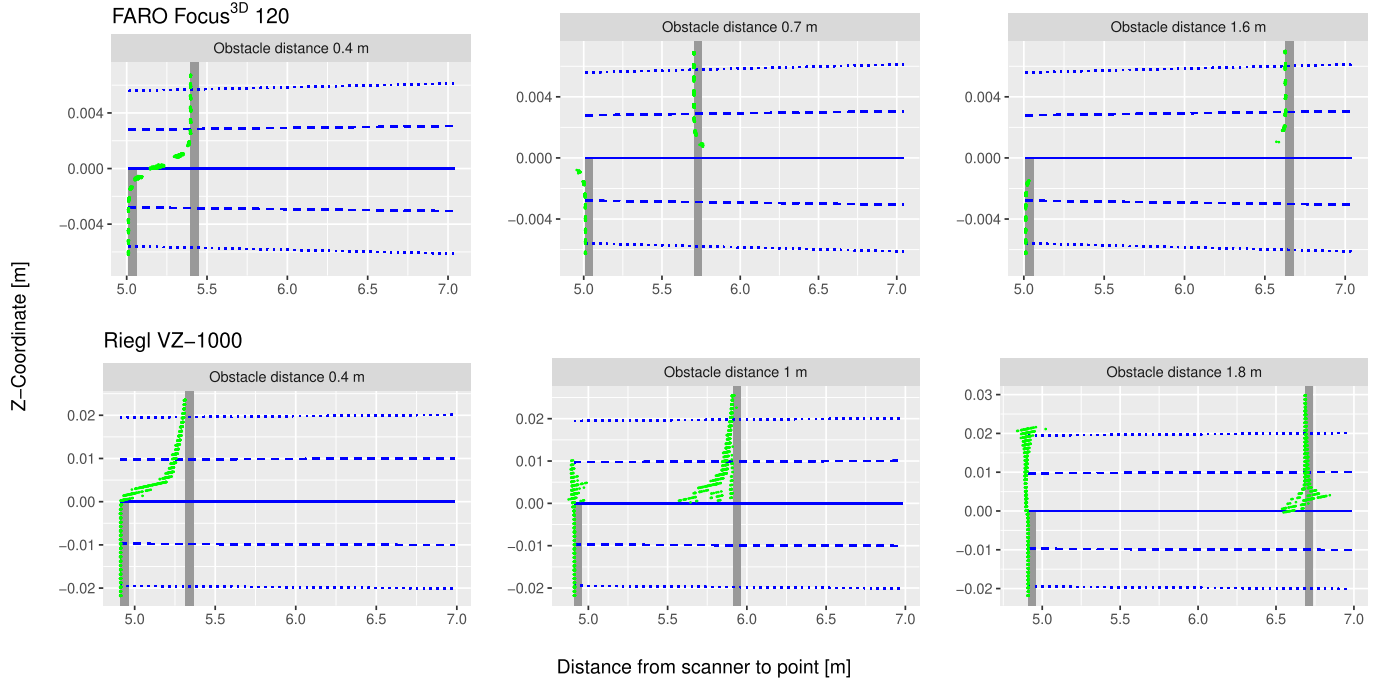
Fig. 2. Side view of point clouds from Riegl VZ-1000 (bottom row) and FARO Focus^{3D} 120 (top row) scanners when the laser beam cones of the scanners intersect with two obstacles. The green dots indicate the triggered echoes (scan points). The blue solid line indicates the center of the view line from the scanner over the edge, and the blue dashed (dotted) lines indicate twice (four times) the standard deviation of the Gaussian-shaped laser beam footprint. Vertical gray bars indicate the positions of the obstacles.

to the closest neighboring obstacle (and a minimal value of at least 1), $\alpha = 1.02$, $\beta = -0.11$, and $\gamma = 90$. γ is used to stretch the model in the x-direction, whereas α and β shift the curve in the x-direction, both influencing the obstacle distance D_o

$$p = \frac{1}{1 + e^{-(E_l - \alpha + \beta D_o)\frac{\gamma}{D_o}}}. \tag{3}$$

b) FARO Focus^{3D} 120: As shown in Fig. 2, the FARO scanner applies four different signal triggering functionalities.

　i *Common Distance Measurement:* A single object placed within the laser beam cone.
　ii *Distance Deviation Through Lack of Object Separation:* The distance is the weighted mean distance of two objects because the following conditions hold: iiA the objects are too close to each other for separation or iiB the objects obtain a nearly identical amount of laser energy and are set wide apart.
　iii Distance deviation through ambiguity in distance measurement.
　iv No signal triggering (filtering).

　i) First, when the laser beam cone intersects with only a single object, no specific triggering model is needed because the distance to the point in the point cloud is the unambiguous distance measured by the laser.

iiA) Second, when the laser beam intersects with two obstacles that are close to each other (0.5 m or less), the scanner does not identify them as separate objects. The distance delivered by the scanner appears to be a weighted mean distance. To derive the model of the distance measurement, we included all points that originated from laser pulses hitting the two obstacles in the lab experiments with at least 2% of

the laser energy. Only the lab experiments where the obstacle distance was between 0 and 0.5 m were selected. We assumed a weighted distance to the two obstacles, as shown in the following equation:

$$D_p = \frac{D_{(1)}e^{\alpha E_{(1)}} + D_{(2)}e^{\alpha E_{(2)}}}{e^{\alpha E_{(1)}} + e^{\alpha E_{(2)}}} \tag{4}$$

where D_p is the distance between the scanner and the point, $D_{(1)}$ and $D_{(2)}$ are the distances from the scanner to the two obstacles, $E_{(1)}$ and $E_{(2)}$ are the ratios of the energy on the respective obstacles, and $\alpha = 4.37$ is the parameter that resulted from the nonlinear least-squares fit of the model.

iiB) Another effect of a lack of object separation occurs when the laser energy on the two obstacles is nearly identical and the obstacle distance is at least 1.8 m. We assumed a weighted mean distance, where the respective laser energies on the two obstacles E_{l_o} serve as the weights

$$D_p = \frac{D_{o1} * E_{l_{o1}} + D_{o2} * E_{l_{o2}}}{E_{l_{o1}} + E_{l_{o2}}}. \tag{5}$$

iii) Third, the other case of distance deviation seems to be dependent on the obstacle distance. The distance deviation oscillates around the edge toward the scanner and away from it. To fit a model, we selected points from around the edge of obstacle 1 of the lab setups with object distances greater than 0.5 m. We assumed, based on effects observed in lab experiments, that the distance deviation depends on a sinusoidal weighted obstacle distance and on the energy ratio of the laser beam on the obstacle. Hence, we set up the model for the distance deviation ΔD as follows:

$$\Delta D = -1 * \frac{\sin\left(\frac{D_o - 0.5}{\alpha} 2\pi\right)}{\beta} * e^{\frac{\gamma}{E_l}} \tag{6}$$

where D_o is the obstacle distance (see Fig. 1) and E_l is the energy ratio of the laser pulse on the obstacle. α gives a weight to the obstacle distance, whereas β weights the sinusoidal effect and γ weights the energy ratio of the laser beam. The latter leads to the effect that the stronger the laser beam hits the object, the smaller the distance deviation becomes. The nonlinear least-squares model fit ended up with $\alpha = 1.324$, $\beta = 65180$, and $\gamma = 5.792$.

iv) Fourth, the last effect we observed in our data (see Fig. 4) is that in certain cases, the FARO scanner does not trigger signals at all, hence prefiltering mixed pixel points with too much ambiguity. This is the case when obstacles are at least 0.6 m apart (meaning that they are identified as separate objects) and the laser energy on both objects is of similar intensity. We assume prefiltering when the energy on the two objects is within the range of 50% ± 20%, based on the observations of the lab data.

c) Riegl VZ-1000: The Riegl VZ-1000 scanner has more complex noise patterns than the FARO and the Leica scanner. This could be due to its ability to trigger multiple echoes from one laser pulse. To describe the noise patterns mathematically, we need to know the exact beam diameter of the Riegl scanner. However, for the Riegl VZ-1000, there is no such specification, neither in its technical specification sheets nor in its manual [28]. The point cloud, however, shows that the scanner produces noise up to 21 mm above the edge of obstacle 1 (see Fig. 2). We assumed a beam diameter at exit of 18 mm ($1/e^2$), as officially specified for the Riegl VZ-4000. In the point cloud of the Riegl VZ-1000 scanner, we observed the following signal triggering functionalities (see Fig. 2).

i *Common Distance Measurement:* A single object lies in the laser beam cone.

ii *Common Distance Measurement of a Laser Pulse Hitting Two Objects:* The laser energy on the first object is above 50%.

iii Multiple signal triggering.

iv Distance deviation through lack of object separation.

v Distance deviation when separate objects are identified with specific. patterns for: obstacle 1 (vA) and obstacle 2 (vB).

i) First, when the laser beam cone intersects with only a single object, no specific triggering model is needed, and the distance of the point in the point cloud is the unambiguous distance measured by the laser.

ii) Second, as shown in Figs. 2 and 4, the Riegl scanner triggers the points on the surface of obstacle 1 if the laser energy reaching it is at least 50% (assuming an equal reflection). Besides this threshold, no specific model needs to be developed.

iii) Third, when the laser beam intersects with the two obstacles, and with obstacle 1 with less than 50% of the laser energy, the probability of triggering two points per laser beam appears to be 100% when the obstacles are at least 1.5 m apart. However, if it is between 0.7 and 1.5 m apart, the probability of triggering two points rises from 0 to 100%, but still only when the laser beam energy on obstacle 1 is less than 50%. The model for the probability of triggering an additional point for obstacle 1, hit with less than 50% of the energy and an obstacle

distance of 0.7 and 1.5 m, is the following, with $\alpha = 0.51$ and $\beta = 2.7$ (nonlinear least-squares fit):

$$P_t = 1 + \alpha \frac{E_{(1)} - 0.5}{D_{(2)} - D_{(1)}} e^{\frac{1}{(D_{(2)} - D_{(1)})^\beta}}. \tag{7}$$

iv) Fourth, when the obstacles are closer to each other than 0.7 m, and in cases where there is no multiple triggering up to an obstacle distance of 1.5 m, the Riegl scanner does not appear to distinguish between separate objects and calculates a weighted mean, similar to the FARO scanner. To capture the effect of the "mean distance," we fitted a nonlinear least-squares model only for the lab data where obstacles were 0.7 m or less apart, as the separation of single and multiple triggered signals between obstacle distances of 0.8 and 1.6 m is difficult, whereas the model presumably remains the same. The resulting model is similar to the model in (4) of FARO, with $\alpha = 4.1$

$$D_p = \frac{D_{(1)} e^{E_{(1)}} + D_{(2)} e^{\alpha(E_{(2)} - 0.5)}}{e^{E_{(1)}} + e^{\alpha(E_{(2)} - 0.5)}}. \tag{8}$$

v) Fifth, once Riegl identifies separate objects, it reveals various patterns of distance deviation (noise pattern) on the two obstacles. To clarify these structures, we separated them from the two obstacles.

vA) If a laser pulse hits obstacle 1 with less than 50% of the energy and a signal is triggered [see model 3)], the points show a specific noise pattern (see Fig. 2). Besides a distance deviation, there is a deviation perpendicular to the laser beam based on the fact that the center of the laser beam is no longer on the object.

We derived an unbiased Gaussian-distributed distance deviation, with a standard deviation of 0.02 m if the obstacles are between 0.7 and 1.1 m apart. If the obstacles are farther apart, the distance deviation from obstacle 1 (ΔD) has the following shape ($\alpha = 27.8$, $\beta = 0.012$, and $\gamma = -0.50$):

$$\Delta D = \frac{\beta}{1 + e^{\alpha(-E_{(1)} + \gamma)}} - \beta \tag{9}$$

with a model for the distance uncertainty (standard deviation) $\sigma_{\Delta D}$

$$\sigma_{\Delta D} = \gamma + \frac{1}{\alpha E_{(1)}^\beta} \tag{10}$$

where $\alpha = 1394$, $\beta = 0.72$, and $\gamma = 0.0022$.

vB) Due to the fact described in ii, only points with laser energy ranging from 50% to 100% on obstacle 2 are triggered for obstacle 2. The distance deviation from obstacle 2 for obstacle distances between 1.1 and 1.8 m is split into two parts: one distance deviation toward the scanner and one away from it. The distance deviation for obstacle distances between 0.7 and 1.1 m is not modeled separately because of difficulties in separating it from the points modeled under iv. The distance deviation was fitted with a nonlinear least-squares approach for the following equation:

$$\Delta D = \alpha(1 - e^{-\beta E_{(2)}}) - \alpha. \tag{11}$$

The noise part toward the scanner obtained $\alpha = 1.3$ and $\beta = 4.7$, and the noise part away from the scanner obtained $\alpha = -0.46$ and $\beta = 2.4$. The corresponding uncertainty for

the distance deviation toward the scanner was fitted with the following model, with the result that $\delta = 0.0089$ and $\gamma = 2.9$:

$$\sigma_{\Delta D} = \delta \frac{1}{E_{(2)}^{\gamma}}. \tag{12}$$

The uncertainty for the distance deviation away from the scanner resulted in $\alpha = 0.00051$, $\beta = 0.0099$, and $\gamma = 13.2$ for the model

$$\sigma_{\Delta D} = \beta + \alpha \frac{1}{E_{(2)}^{\gamma}}. \tag{13}$$

Beyond an obstacle distance of 1.8 m, we observed a constant distance noise depending on the energy on obstacle 2, as in (12), with $\alpha = 0.01$ and $\gamma = 2.4$.

C. Simulation Study: Laser Scanning for Forest Inventories

1) Stand Models Based on Swiss National Forest Inventory (NFI) Data: Swiss NFI data are collected on a systematic grid covering the entire country. This makes it possible to make a statistical inference regarding population values, such as wood volume, for the area of interest, e.g., for a whole country [29]. Since 2009, field measurements for the Swiss NFI have been conducted on nine systematic subgrids of equal size. This enables representative evaluations of either single or combined grids.

As in an earlier study [21], we used information about the measured trees with heights of at least 1.3 m to derive stand-describing parameters in the form of a Weibull distribution. The variability of the derived stand descriptions covers all the possible stand parameters that are likely to occur in Swiss forests and includes some extreme values as well.

2) Stand Models for Simulation: We implemented the stand models in the same manner as in one of our previous studies [21], using Blender and the stand parameters to set up cylinders as a proxy for tree stems, with a position and a diameter, for a horizontal scan. Mixed-signal effects are based on laser beams hitting multiple objects, and the goal is to have the same for cylinders at the edge of the sample plot. We therefore at least doubled the edge length of our square sample plots compared with the size of the plot we used for the evaluation. Because the time needed for the definition of new cylinders increases exponentially, we limited the number of cylinders in a scene to 4000, unlike in [21]. However, in order to simulate dense stands as well, we applied simulations to two different rectangular plot sizes, with edge lengths of 23 and 100 m, to evaluate plots with the edge lengths of 10 m for plots with tree densities above 4000 trees per hectare and with 50-m edge lengths for plots with tree densities below 4000 per hectare.

3) Signal Triggering Models: The goal of the simulation study is to simulate the most important effects when laser beam cones of TLS systems intersect with multiple objects. In this section, we describe the approaches used to simulate TLS systems based on our lab observations. As mentioned in Section II-A, we sampled the footprint of a circular-shaped virtual laser pulse based on a Gaussian-shaped density across the beam energy distribution. In Blender, one can set the angular resolution in longitudinal or latitudinal directions. In our study,

we set both angular resolutions to 0.04°. The sampling rate for one laser pulse was set to 300 sampled distances. The sampling rate has an influence on the sensitivity of the simulated laser scan at the fringes of the laser footprint. For our simulation study, we implemented different kinds of models derived from the lab tests but also some theoretical approaches as a "baseline" for comparison purposes. All the models have in common that they deliver a distance from the scanner. Knowing the longitudinal and the latitudinal direction of the laser beam center, the combination with the distance to the scanner makes it possible to calculate a point in the point cloud.

The first step in the simulation of signal triggering was to identify possible objects for each laser pulse based on the range measurements of the samples ($n = 300$) within the respective laser beam cones. For this purpose, we counted the number of range measurements within a 0.2 m window, moved in 1 mm steps from the minimal measured distance within the laser pulse to the maximal measured distance. Within this array of 1-mm steps, we identified the local maxima. These local maxima, their locations, and the number of samples assigned to them provide a rudiment of objects, their ranges, and the amount of laser pulse energy hitting them. In this study, these rudiments of objects are named "proto-objects." The amount of laser energy hitting a proto-object (referred to as E_I) is the ratio of the number of range samples closest to the respective proto-object (local maximum) to the total number of distance measurements sampled within one laser pulse.

a) Geometric scanning: "Geometric scanning" is a theoretical approach that stands for a scanner with an infinitesimally small laser beam diameter. In the simulation, this means that one only samples the main direction of the virtual laser beam with one sample. This distance measurement is not subject to any distance deviation or other noise effect. It serves as a "baseline" to compare the performance of the other scanning approaches.

b) Mean distance: The "mean distance" scanner is a theoretical approach as well. It represents a very primitive (nonexistent) LiDAR scanner that simply produces a mean distance to the obstacles that are hit by a laser pulse. It serves as a "worst case scenario" comparison with the other approaches.

c) L-system: A Leica-like LiDAR simulation: The lab experiments of the Leica BLK360 scanner reveal only pre-filtering as an effect of laser pulses hitting multiple objects. Prefiltering of points produced by a laser scanner is always based on ambiguous backscattered signals from a LiDAR distance measurement. Ambiguous signals reduce the probability of triggering a signal. We implemented a prefiltering model, i.e., a model for triggering probability based on the lab data from the Leica BLK360 scanner (see Section II-B3). In the simulation, the prefiltering model first derives the proto-objects for each laser pulse. If there is only one proto-object within one laser pulse, the distance to that object is taken directly. If multiple proto-objects are in the way of a laser beam, the model checks the triggering probability for the proto-object that obtained the most energy from the laser pulse, according to the triggering probability function in (3). The input parameters for the model are the energy ratios of the

R-system

```
Identify proto-objects (Oₚ)
```

```
Intersection with multiple Oₚ?
```

yes — no — i

```
E_{p(1)} > 50 %?
```

no — yes — ii

```
Group Oₚ with distances < 0.75 m, to
identifiable-objects (O_id)

Decide on separate triggering (and further
grouping into O_id) for O_id with distances
< 1.5 m, according to iii.
```

```
For each O_id: are multiple Oₚ in O_id?
```

no — yes — iv

```
Is E_{id(1)} > 50 %?
```

no — yes — ii (keep distance
calculated in iv)

```
Is O_id closest to scanner?
```

no — yes

vB — vA

F-system

```
Identify proto-objects (Oₚ)
```

```
Intersection with multiple Oₚ?
```

yes — no — i

```
Group Oₚ with object distances < 0.55 m to
identifiable objects (O_id)

Identify O_id with most Energy (E_id)
(O_id* and E_id*)
```

```
Is O_id* composed of multiple Oₚ?
```

no — yes — iiA

```
Is E_id = mean(E_id) +- 5% and object
distances > 1.8m?
```

no — yes — iiB

iii

```
Is E_id* = mean(E_id) +- 20%?
```
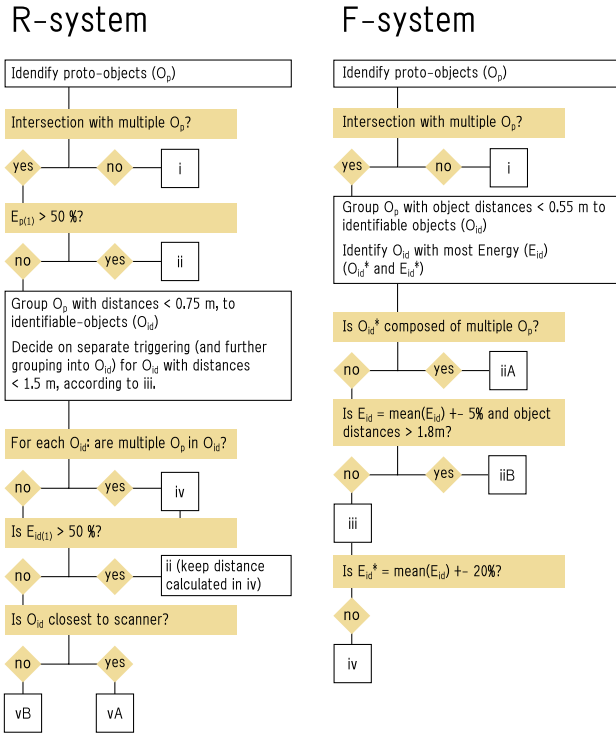
no

iv

Fig. 3. Decision tree on signal triggering of R- and F-system. O_p are the proto-objects, and E_p is the according energy ratio on each proto-object. O_{id} are the identifiable objects, whereas one O_{id} can be composed of either one or several O_p. E_{id} is the cumulative energy ratio on all O_p within each O_{id}. Procedures i, ii, iii, iv, vA and vB for the R-system and i, iiA, iiB, iii and iv for the F-system, are described in the text.

laser pulse on this proto-object (E_I) and the distance to the closest neighboring proto-object D_o. However, we limited the values of D_o to a minimum of 1 m and a maximum of 8 m to produce plausible probabilities with the trigger probability function.

d) F-system: A FARO-like LiDAR simulation: We implemented the observed scanner properties in the following manner in order to handle multiple objects in the direction of the laser beam (see Fig. 3). The bases for applying the models are the "proto-objects," with their corresponding distance and energy ratios of the laser pulse reflected by each object. According to our observations, the FARO scanner does not separate objects within one laser pulse that are less than 0.55 m apart but treats them as one [the threshold lies between 0.5 and 0.6 m, according to the laboratory tests, see Fig. 2 (left)]. Therefore, we grouped the proto-objects together if they were less than 0.55 m apart and called them "identifiable-objects." Within these groups, we summed the reflected laser energy and calculated the mean distance to the proto-objects within the groups. We observed that the FARO scanner only triggers one signal per range measurement. Because this happens on the object that reflects the most energy, we selected the identifiable-object with the most laser energy. In cases where multiple objects had the same amount of energy, we selected the one closest to the scanner. In addition, we selected the identifiable object with the second most energy reflection. As the last preparatory action, we calculate the average energy of all the identifiable objects. Based on this

information, we implemented the following triggering models (see Section II-B3).

i) If there is only one proto-object in the laser beam cone for the range measurement, this distance is taken.

iiA) If the identifiable object with the most energy is composed of multiple proto-objects, the weighted mean distance of the proto-objects according to (14) is calculated ($\alpha = 4.37$). This distance might be subject to prefiltering.

$$D_p = \frac{\sum_{i=1}^{n} D_{(i)} e^{\alpha(E_{(i)}-0.5)}}{\sum_{i=1}^{n} e^{\alpha(E_{(i)}-0.5)}} \quad (14)$$

where D_p is the distance between the scanner and the point, $D_{(i)}$ are the distances from the scanner to the n proto-objects, and $E_{(i)}$ are the ratios of the laser energy on the respective proto-objects.

iiB) If all identifiable objects are farther from each other than 1.8 m and reflect a laser beam energy that is within $\pm 5\%$ of the average energy on all identifiable objects, a simple mean distance, weighted by the respective energies of the identifiable objects, is calculated according to (5).

iii) If the identifiable object with the most energy contains only one proto-object, but the laser beam cone intersects with multiple identifiable objects, the distance measurement is subject to a distance deviation according to the model described in (6). As the distance between the obstacles (D_o), the distance between the two identifiable objects with the most energy is taken. The laser pulse energy can also be distributed across more than two objects, and the model input of laser energy was therefore adjusted so that the possible range of energy on the identifiable object is 70%–100%, which are the energy values that the model is fitted on. The slight intercept of this model when 100% of the energy is reached is removed from the distance deviation. In addition, the amount of energy (E_l) is set to a minimum of 70% so that the derived model produces plausible values. These signals are subject to prefiltering as well.

iv) *Prefiltering:* If the energy of the identifiable object with the most energy is less than the average energy of all identifiable objects plus 20%, no signal is triggered. The idea behind this approach is, with reference to observations in the lab experiments, that if the energies on the objects are too close to each other, the scanner omits the echo. Thus, we assume that if the identifiable object with the most energy is too close to the average energy, ambiguity has been reached for the scanner.

e) R-system: A Riegl-like LiDAR simulation: Fig. 3 shows the implemented signal triggering for the Riegl like system. Similar to the FARO scanner, there is a minimal distance at which the Riegl device does not appear to distinguish between two objects. In the lab experiments, this threshold is very clearly visible up to an obstacle distance between 0.7 and 0.8 m. Therefore, we grouped proto-objects that were closer to each other than 0.75 m into "identifiable-objects" and calculated their mean distance to the scanner and the energy ratio of the laser beam hitting the proto-objects within each identifiable-object. However, also beyond this distance up to 1.5 m, depending on whether the scanner performs
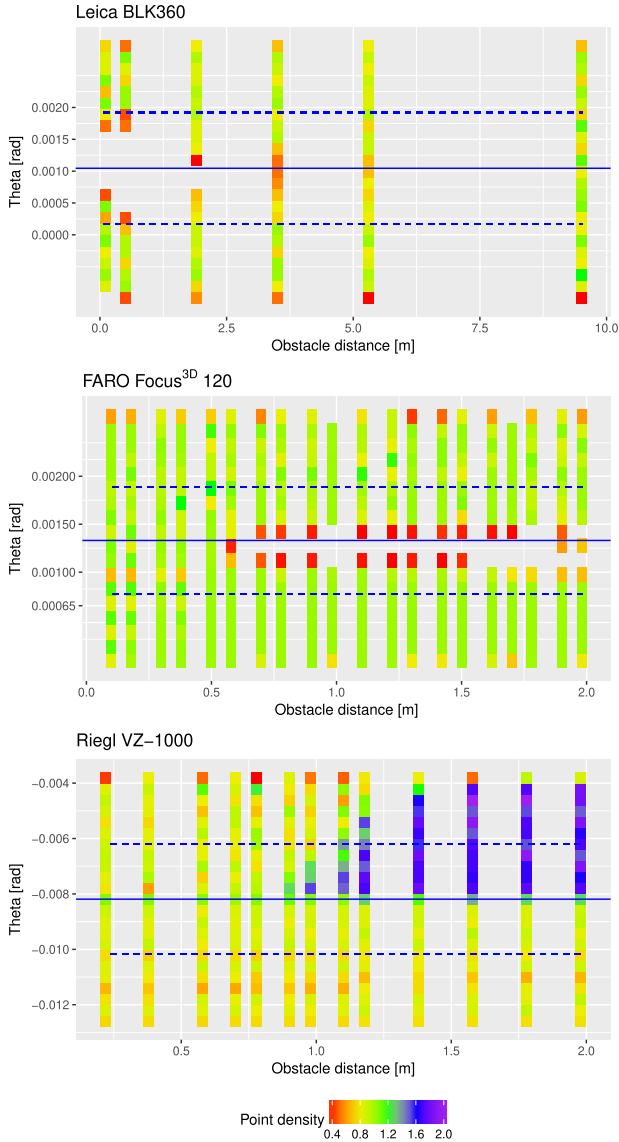
Fig. 4. Prefiltering and multiple triggering from lab tests of three different scanners [(Top) Leica BLK360, (Middle) FARO Focus³D 120, and (Bottom) Riegl VZ-1000]: point densities per scanning angle (theta) from multiple experimental setups as a function of obstacle distances. The blue solid line shows the view line of the scanner at the edge height of obstacle 1. The blue dashed line represents the footprint (using $1/e^2$) when the beam center is at the edge height of obstacle 1. Colors on the vertical bars indicate point densities.

multiple triggering, the Riegl scanner does not appear to distinguish between these obstacles, with decreasing probability. For multiple-signal triggering, we checked whether the identifiable objects are closer to each other than 1.5 m. In the lab experiments (see Fig. 4), the Riegl scanner always triggers multiple signals when obstacle distances are beyond this value. When they are smaller, it triggers with increasing probability. We implemented the following signal triggering models for the R-system (see Section II-B3).

i) If the laser pulse for the range measurement hits only one object, the range measurement to that object is used to directly calculate the coordinates of the point.

ii) In the lab experiments (see Figs. 2 and 4), the Riegl scanner triggers a point clearly on the first obstacle

that the laser beam hits, as long as the laser beam energy on this obstacle is above 50%. Consequently, we implemented the same logic for either the proto-objects or the identifiable objects, with their specifically calculated distances [see iv)].

iii) Multiple-signal triggering is implemented as follows [considering ii)]. As shown in Fig. 4, the Riegl scanner always triggers a signal for each obstacle if they are farther from each other than 1.5 m. We implemented this rule for each "identifiable object." However, when the obstacle distance is between 0.7 and 1.5 m, the probability of triggering signals for separate obstacles continually rises from 0% to 100%. The implementation of multiple-signal triggering for groups of identifiable objects when they are between 0.7 and 1.5 m apart is as follows. The identifiable object with the most energy is definitely triggered. The probability (p) of triggering a signal for the other obstacles (identifiable objects) is

$$p = 1 + \alpha * (E_{\text{within}} - 0.5) * \frac{1}{D_{\text{meo}}} * \exp^{D_{\text{meo}}^{-\beta}} \quad (15)$$

where $\alpha = 0.51$, $\beta = 2.7$, E_{within} is the relative energy of the laser pulse on all identifiable objects that are 0.7–1.5 m apart and are intersected by one laser pulse, and D_{meo} is the distance to the identifiable object with the most energy. When p is below 0, it is set to 0.

iv) The lab experiments indicate that obstacles closer to each other than 0.75 m are not distinguished as separate objects. Also, beyond that obstacle distance, up to 1.5 m, the scanner does not appear to always distinguish between separate objects, although with decreasing probability. This probability appears to be connected to the triggering of multiple signals with one laser pulse. Thus, if the scanner identifies separate objects, it triggers points for each obstacle; otherwise, it treats them as the same object. In that case, the scanner interprets multiple proto-objects as a single object and calculates a weighted mean distance. We implemented the calculation of the weighted mean distance to the obstacle D_p based on (8) in the following way:

$$D_p = \frac{D_{(1)}e^{E_{(1)}} + \sum_{i=2}^{n} D_{(i)}e^{\alpha(E_{(i)}-0.5)}}{e^{E_{(1)}} + \sum_{i=2}^{n} e^{\alpha(E_{(i)}-0.5)}} \quad (16)$$

where $D_{(i)}$ are the distances from the scanner to the (1 to n) obstacles and $E_{(i)}$ is the amount of laser pulse energy on the (1 to n) obstacles, with $\alpha = 4.08$.

vA) The obstacle closest to the scanner shows two patterns of distance deviation for points triggered from laser pulses intersecting the obstacle with less than 50% of the energy and hence with their center not on the obstacle itself. Depending on the distance to the next obstacle, this distance deviation gradually develops a specific pattern (see Fig. 2). We split this gradual development into two specific patterns: one for obstacle distances below 1.15 m and one for obstacle distances beyond 1.15 m.

At obstacle distances below 1.15 m, we assumed a constant normally distributed distance deviation with

a standard deviation of $\sigma = 0.02$ m. For obstacle distances beyond 1.15 m, a distance deviation is directly implemented with (9) for the shape and with (10) for the uncertainty.

vB) Fig. 2 shows different distance deviation patterns on obstacle 2. To be close to the output of the lab experiments, we implemented the distance deviation pattern as follows. The case where obstacles cannot be distinguished is already treated under iv). Once multiple triggering takes place, a gradual change occurs in the pattern of obstacle distances from 0.7 to 2 m, beyond which it appears to remain constant. We thus implemented the distance deviation pattern for the obstacles that are not hit first by the laser pulse with two models: one for obstacle distances below 2 m and another for obstacle distances above 2 m. For the distance deviation of identifiable obstacles with a distance of less than 2 m to the next object, we split the range measurements into two equally sized groups: one deviating toward the scanner and the other away from the scanner. For the shape of these distance deviations, we used (11) and the corresponding standard deviations in (12) and (13) for a Gaussian-shaped distance uncertainty of the deviation toward the scanner and away from it. When the laser energy $E_{(l)}$ on one of the objects drops below 50%, it is set to 50%.

If an identifiable object is at least 2 m away from the next object, (12) is used again, with $\alpha = 0.01$ and $\gamma = 2.4$ for an unbiased distance noise, dependent on the energy on the respective object.

4) Simulated Laser Scanner Types and Beam Properties: We implemented the above-described LiDAR simulation approaches, except for the "geometric scanning," with beam diameter sizes at exit $(1/e^2)$ of 3, 18, and 50 mm, following the diameters described in Table I. The idea was to have a small and a large TLS version and a diameter that represents a footprint of a drone-mounted LiDAR scanner. As a beam divergence, we implemented 0.3 mrad for all simulations.

5) Simulation Control, Data Preparation, and Statistical Analysis of Simulation Output: The simulations were implemented in Blender [20], as adapted in [22] and described in this publication. We used Blender to simulate diameter distributions from one annual panel (representative grid) of the Swiss NFI, as described in [21]. Each of these scenes was virtually scanned with the abovementioned scanner models with different beam diameters. This led to a total of 8890 2-D point clouds. For the evaluation, we used the true position and the diameters of the cylinders in the scene to assign the points from the point cloud to the closest cylinder. In real TLS applications, point clouds are usually filtered in order to remove possible noise, e.g., from mixed pixel echoes, or points of unwanted objects, e.g., leaves in case woody volume is targeted. The filtering procedure depends to a large extent on the scanned objects, the evaluation routines, and the goal of the scanner application. As a proxy for noise filtering, we implemented a simple filter procedure, removing all points farther than 2 cm and 10% of the cylinder diameter from its surface. This filtering approach is not applicable in

real scanning situations, as it needs *a priori* knowledge on the objects, but was used here to illustrate possible filtering effects, as well as the influence of noise points with large distance deviations. All statistical analyses were performed in R (Version 3.4.4) [30].

III. RESULTS

A. Analysis of Edge Noise Effects of Three Terrestrial Laser Scanners

Edge noise effects of three terrestrial laser scanners (Leica BLK360, FARO Focus³ᴰ 120 and Riegl VZ-1000) were analyzed using the experimental setup, as shown in Fig. 1. The distances between the obstacles intersected by one laser pulse play a major role in how these devices trigger one or multiple points, as our observations of their point clouds indicate. The distance between obstacles, as used in our experiments, had to be adapted for each individual device because every device triggers points in a unique way. To simplify the experimental approach and modeling, we only used two obstacles.

1) Prefiltering: One aspect of the triggering functionality is how the devices omit echoes (prefiltering). Fig. 4 shows the number of echoes (points) triggered per laser pulse sent out by the laser scanner in a specific latitudinal direction (theta). The Leica scanner omits echoes from multiple obstacles that are close to each other such that the energy of the laser pulse is similar on both objects. The closer the objects are, the stronger the prefiltering is. The FARO scanner also performs prefiltering when the energy on both obstacles is similar, but from an obstacle distance of around 0.5 m and greater. With increasing distance between the obstacles, prefiltering becomes slightly stronger. At an obstacle distance greater than 1.8 m, however, and only when the laser pulse energy on two objects is almost the same, the prefiltering intermits.

2) Multiple Triggering: Neither the FARO nor the Leica scanners trigger multiple points from one laser pulse. On the other hand, the Riegl scanner does no prefiltering at all but supports multiple triggering. Multiple triggering is referred to here as the triggering of more than one point per laser pulse. Time-of-flight laser scanner systems have the ability to trigger multiple signals from one laser pulse [12], [31]. As shown in Fig. 4, the Riegl VZ-1000 triggers more than one point per laser pulse for specific obstacle setups. Up to 50% of the laser pulse energy on the first obstacle reflected by it leads to clear triggering on the first obstacle. If the energy is less than 50% when the laser beam center has crossed the edge, and the obstacles are more than 0.7 m apart, the scanner begins to trigger echoes from both obstacles with increasing probability, reaching 1 when the obstacles are more than 1.5 m away from each other. Beyond this obstacle distance, two signals are always triggered when a laser beam intersects with two objects.

3) Distance Deviation Through Lack of Object Separation: The placement of obstacles intersected by one laser pulse of a scanner influences not only prefiltering and multiple triggering but also where a point is triggered. A user of laser scanners expects the points to represent points on the surface of scanned objects. However, depending on the surface a laser

pulse hits, the time-dependent profile of the backscattered light (waveform) is altered (see [32]). Based on this waveform, the scanner has to decide whether it has hit one or more objects with one laser pulse. With strong prefiltering, the Leica scanner removes most of the ambiguous distance measurements so that only signals that lie fully on the object surface are triggered (except for the common range noise). In very rare cases, as can be observed in Leica point clouds, this is not the case. However, as we can see in Fig. 2, the FARO and the Riegl scanners do not distinguish between two objects if they are close to each other. When the obstacle distance is small, these scanners trigger the points at something similar to a weighted mean distance of the laser beam to the obstacles [see Fig. 2 (left)]. With increasing distance between the objects, points are triggered at the distance of either one of the two objects (or both as in the case of multiple-signal triggering). The distance threshold is up to 0.6 m for the Riegl scanner and 0.5 m for the FARO scanner. Beyond these obstacle distances, the scanners produce separated point clouds for different obstacles. However, even with higher obstacle distances (e.g., 1.8 or 2 m) and when the laser beam center hits the edge of obstacle 1 exactly, the FARO scanner appears to have problems separating the two obstacles.

4) Distance Deviation Through Mixed Pixel Effects: As we observed in the lab experiments, FARO Focus^{3D} 120 and Riegl VZ-1000 produce specific range deviations when the laser beam cone intersects more than one object and the scanner is able to distinguish between two objects (see Fig. 2). The FARO scanner triggers points on either object, starting at a distance between obstacles of 0.6 m. It produces a slight distance deviation of the triggered points, sometimes toward the scanner, sometimes away from it, in a sinusoidal manner depending on the distance between the obstacles.

The distance deviation of the Riegl scanner displays a more complex pattern. The Riegl device triggers points "exactly" at the surface of obstacle 1 when the laser pulse energy on it is greater than 50%. However, there are scan points above the edge of obstacle 1, due to the ability to trigger multiple signals for one laser pulse (see Fig. 2). This begins to happen when the laser energy on the first obstacle is less than 50% and the obstacle distance is at least 0.8 m, with an increasing probability of triggering with increasing obstacle distance, reaching 100% when the obstacles are 1.4 m apart. In addition, these points slightly deviate toward the scanner by a few centimeters. The points on obstacle 2 deviate in both directions depending on the laser pulse energy on this obstacle. The pattern of the noise on obstacle 2 changes for obstacle distances of up to 2 m. Above that distance, the pattern remains constant (depending on the laser pulse energy ratio on obstacle 2).

B. Analysis of Simulation Study

1) Impact of Laser Beam Diameter and Object Size on Visibility: Our hypothesis (see Section I) was that beam diameter and signal triggering have an influence on the detection of objects. For forest inventories, it is crucial to know which object size is still detectable, as this makes it possible to set realistic objectives when applying close-range laser scanning. We defined "detectable" objects as those that have at least one laser point assigned (closer to their surface than to the surface of another object). We simulated laser scanning in a plane with different beam diameters and signal triggering approaches, where cylindrical objects following stand densities derived from 684 NFI sample plots were placed as detectable objects. To show the effect of filtering procedures on the point cloud, we removed points that were more than 10% of the cylinder diameter and at least 2 cm away from the cylinder surface.

Fig. 5 shows the comparison regarding the mean detectability of different object sizes by laser beam diameter and signal triggering from 514 square sample plots with edge lengths of 50 m and tree densities below 4000 trees per hectare. Each signal triggering approach is compared with a geometric scanning, which represents a laser scanner with an infinitesimally small laser beam. Such a theoretical scanner would deliver a point cloud without any noise or distance deviation from the objects. We also implemented a system "mean distance," which calculates the mean distance weighted by the reflected energy to all the objects that are hit by a laser pulse. This system represents the opposite of the geometrical approach and delivers a maximum amount of noise. The most important effect is that the smaller the beam diameter, the higher the detection rate of small objects, especially in dense plots (see Fig. 7). When only one point per laser pulse can be triggered, small objects up to at least 4 cm in diameter are clearly less frequently detected. The reason for this effect is that when multiple objects are hit by one pulse, the larger objects reflect more light, which favors their identification. In the case of scanning systems with prefiltering (L-system or F-system), this effect can lead to a further loss of points for small objects. On the other hand, systems with multiple triggering abilities, as implemented in the R-system, show a clearly higher rate of object detection. If a scanner system were to use the "mean distance" approach, the detection rate without filtering would be at the same level as with multiple triggering (R-system) or even higher. Yet, as the detection rates after filtering in Fig. 5 indicate, most of the objects are false detections. This implies that many of the points for small objects would not contribute to a reasonable reconstruction of a scanned object. The "visibility" of an object depends strongly on the object size, the distance to the scanner, and the stand parameters (e.g., the density of objects). Thus, with shorter distances from the scanner, for example, for squares with edges 10 m in length, more objects are detected, even with a higher "tree density." Especially, small objects are less occluded when scanned with small laser beam diameters, as shown in Fig. 7.

2) Impact of Laser Beam Diameter and Object Size on the Representation of Scanned Objects: The number of points by which an object is represented in a point cloud, and the precision of their location, are crucial for the assessment of using laser scanning. We, therefore, evaluated the number of points per object (cylinder) with and without filtering. The filtering is described in Section III-B1. "Invisible" objects, that is, objects with no points after filtering, were not considered
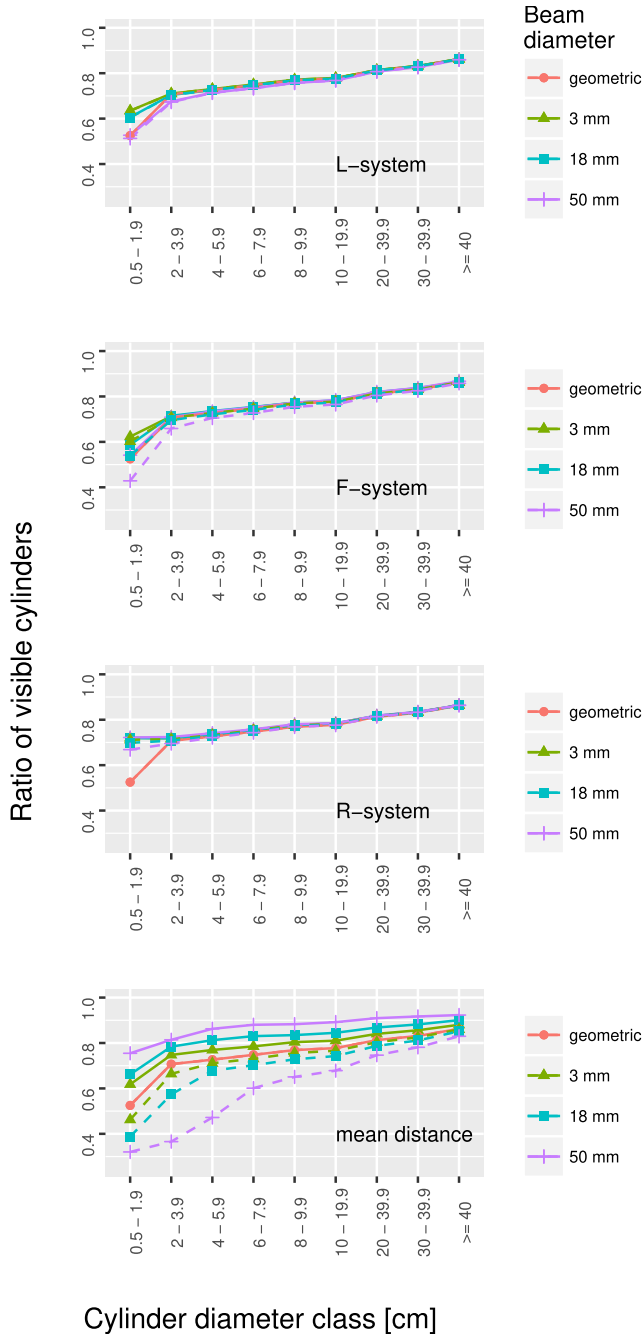
Fig. 5. Ratio of the number of cylinders with at least one "hit" to the total number of cylinders on 514 square plots with an edge length of 50 m in forest stands with a tree density of less than 4000 trees per hectare, by cylinder diameter class, signal triggering model, and laser beam diameter at exit. Dashed line: number of visible cylinders after filtering the point cloud.

Fig. 6. Number of points per cylinder in simulation experiments for 514 square sample plots of 50×50 m in forest stands with tree densities of less than 4000 trees per hectare. Only cylinders that have at least one point in all the simulated scanning settings are evaluated. The box plots show the variation in the number of points per cylinder for different cylinder diameters, point triggering models, and laser beam diameters at exit from the scanner. The red dots indicate the median of the number of points after filtering the point cloud (points must be closer than 10% of the cylinder diameter and, if not, closer than 2 cm). The point triggering model "geometric" simulates a laser scanner with an infinitesimally small laser beam.

in the evaluation. The filtering serves as an indicator of the quality of the precision of the points' locations. Fig. 6 shows the variation in the number of points as boxplots. It only compares objects that have at least one triggered echo in each of the scanning approaches. The variation arises from the distance to the scanner and the stand parameters, especially the density of the objects (see also [21]). A regression analysis using the following formula demonstrates the importance of the influence of the objects' diameters, their distances from
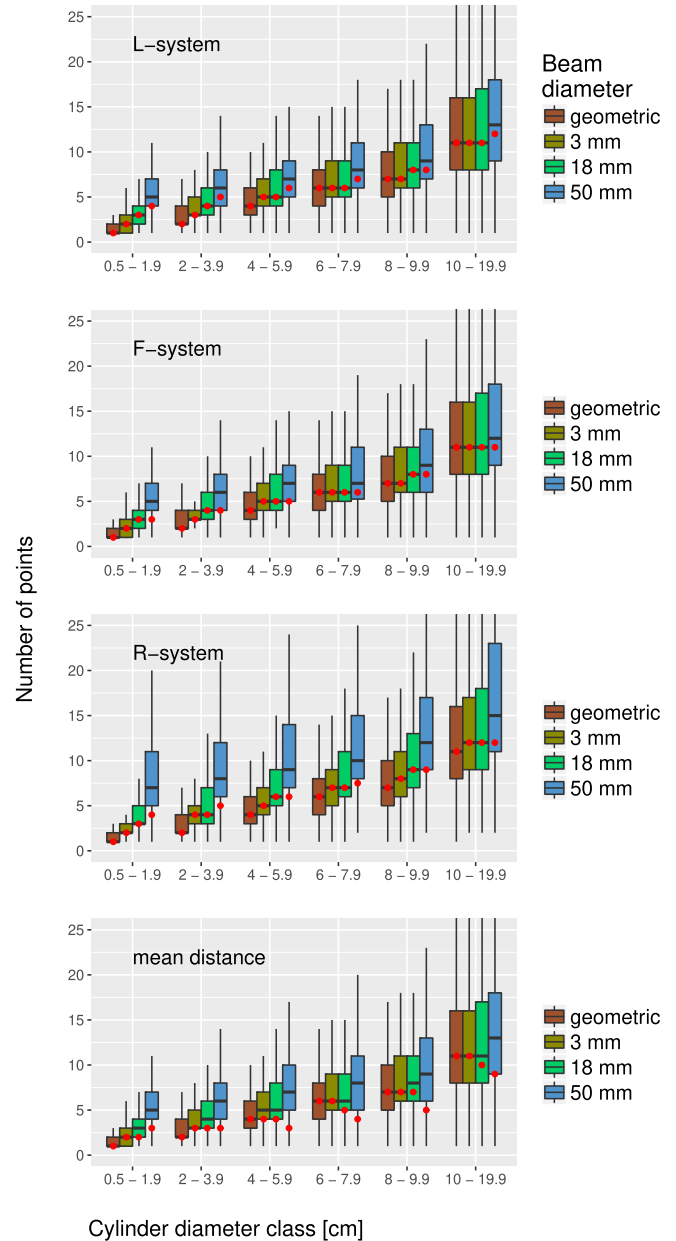
the scanner, and the number of objects per scene:

$$\sqrt{n_p} = \log(\text{diam}_o) + \log(D_s) + \sqrt{n_t} + \text{prop}_L \qquad (17)$$

where n_p is the number of points per object, diam_o is the diameter of the objects (cylinders), D_s is the distance between the object and the scanner, and n_t is the number of objects per scene and indicates the density of objects. As we have shown previously (see [21]), n_t is the most important stand parameter that influences the visibility of a sample plot when

TABLE III

Standardized Model Coefficients Based on Scaled Variables to Make Their Effect Size Comparable, for the Diameter of the Objects (Cylinders) $diam_o$, the Distance Between the Object and the Scanner D_s and the Number of Objects (Trees) n_t. Adjusted $R^2 = 0.69$

Variable	Standardized model coefficient	p value
Intercept	0	0
$log(diam_o)$	0.59	0
$log(D_s)$	-0.58	0
$\sqrt{n_t}$	-0.16	0

performing laser scanning. To show the effect of these three influencing parameters, we removed the influence of the LiDAR property $prop_L$ (signal triggering system and beam diameter) by including it in the model.

In dense stands (see Fig. 8), the L- and F-systems have fewer points per object with increasing laser beam diameter, especially on small objects. However, in stands with lower tree density, a larger laser beam diameter leads to more points per object. The R-system, which is capable of multiple-signal triggering, displays a significant discrepancy between the unfiltered and the filtered point cloud for large footprints. In the point cloud without filtering, the number of points is far greater and wrongly suggests that a large footprint performs better than a small one. This indicates that point location precision is suboptimal. All plots in Fig. 6 suggest that there are limits to object sizes that are reasonable to scan, depending on the scanning system, the beam diameter, and the application. As can be seen in Fig. 8 and also suggested in Table III, scans from closer objects deliver a much greater number of points per object, even for smaller sizes.

IV. Discussion

The objective of this simulation study was to investigate the effects of certain TLS properties, such as laser beam diameter and signal triggering, on point cloud quality when scanning in forested environments. For the implementation of a TLS simulation, we analyzed three state-of-the-art terrestrial laser scanners in terms of their effects when their laser beams intersect with multiple objects along their range. The findings from this study provide a basis for setting realistic objectives regarding the application of TLS for forest inventories.

The presented simulations make it possible to partially explain how the various scanning effects of the three devices influence the resulting point cloud. These effects are the prefiltering of points based on ambiguous echoes, the distance deviation patterns at edges of objects, the lack of separation of objects, and the triggering of multiple points per range measurement. The simulation study reveals the extent to which laser beam diameter and signal triggering approaches influence point cloud quality. The main implications are that objects with "small" diameters can hardly be depicted by TLS in a reasonable way because they are not visible in the point cloud, represented by very few echoes, and/or subject to severe measurement errors due to ambiguous echoes (edge effects). The actual threshold for "small" depends on the objective of the TLS application and the point cloud evaluation algorithms applied.

The lab experiments demonstrate two effects of deviation of scan points from an object's surface: one perpendicular to and the other parallel to the laser beam. The perpendicular deviation is an effect of multiple-signal triggering, which produces points along the central axis of the laser beam. Thus, if a beam touches an object at its edge, the point's possible distance to the object is directly dependent on the diameter of the laser. Concerning the distance deviation parallel to the laser beam, the phase shift system (FARO) performs differently compared with time-of-flight systems (Riegl and Leica). The phase shift system struggles with ambiguity problems, due to the combination of intensity modulations in the laser beam to measure a range. Therefore, depending on the distance of the scanned obstacles to each other, it can either remove points that are clearly problematic (prefiltering) or display a distance deviation that is sinusoidally weighted by the distance between the obstacles. In certain cases, ambiguities cannot be resolved and produce severe distance deviations (range averaging as described in [14]). Time-of-flight systems do not struggle with this kind of problem, due to their ability to evaluate the whole reflected laser energy pattern over time. The Riegl and FARO scanners do not separate obstacles that are close to each other, whereas the Leica scanner solves the problem by prefiltering these points. For a scanning device, there is no way to perfectly resolve all types of objects of any shape, as one object with an inclined surface may reflect the same light pattern as two separate objects. There are only two available options, to either prefilter or provide some kind of average distance to the objects (range averaging, see [14]).

The simulation study shows the limitations of depicting small objects precisely in a point cloud. Either they are not visible or they have only very few points because of their small size. Especially when a scanner prefilters the point cloud, almost no points are left on small objects. Triggering multiple signals alleviates this effect, whereas the points are at a certain distance from the object surface, which can lead to erroneous object reconstructions. Another observed effect is that objects appear flattened in the point cloud with increasing beam diameters. This effect is due to the laser beam working like a moving window, averaging the ranges measured within its footprint.

The signal triggering of laser scanning systems is influenced by many factors, such as the object shape, its surface, the reflectance of the object, the constellation of multiple objects, and even the atmospheric conditions. In addition, the scanner settings (adjustable or not) have an influence on the point cloud. However, reverse engineering of signal-triggering functionalities, without any detailed manufacturer's information on the devices, is a huge effort. Nevertheless, we were able to cover the most important effects observed in point clouds.

The effects observed with the two-obstacle lab setting had to be generalized for cases where a laser pulse hits more than two objects. Hence, the effects caused by such settings most likely
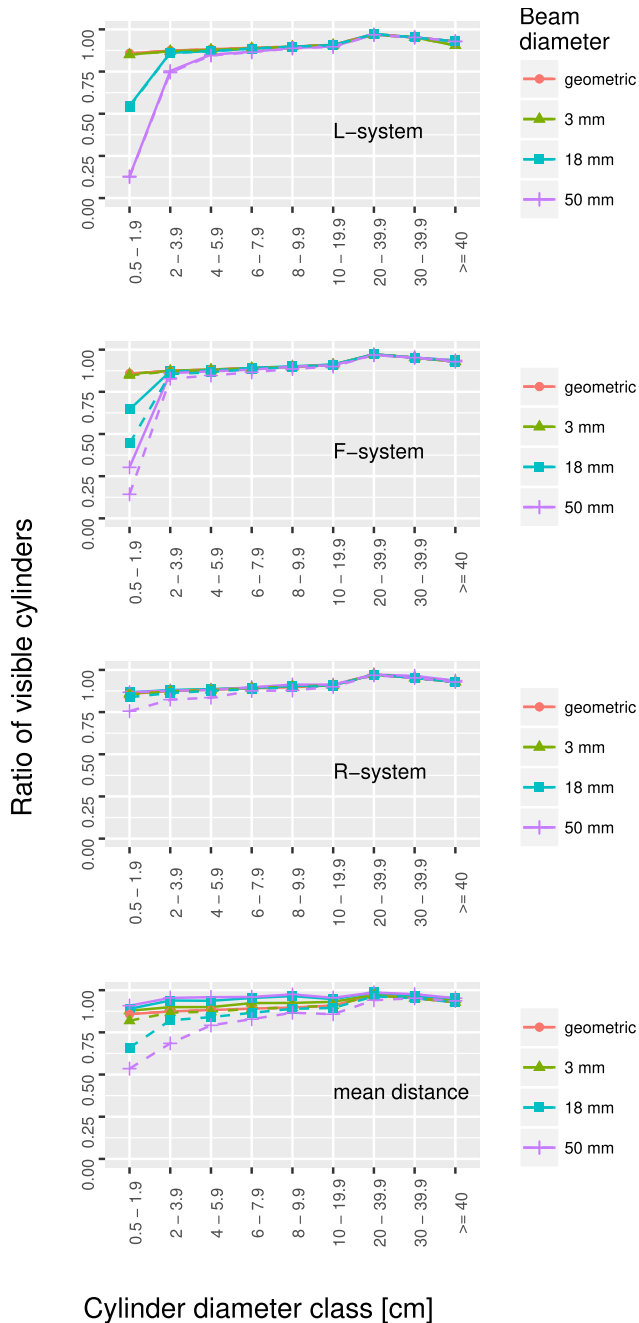
Fig. 7. Ratio of the number of cylinders with at least one "hit" to the total number of cylinders on 170 square plots with an edge length of 10 m in forest stands with tree densities of more than 4000 trees per hectare, by cylinder diameter class, signal triggering model, and laser beam diameter at exit. Dashed line: number of visible cylinders after filtering the point cloud.

Fig. 8. Number of points per cylinder in simulation experiments for 170 square sample plots of 10 × 10 m in forest stands with tree densities of more than 4000 trees per hectare. Only cylinders that have at least one point in all the simulated scanning settings are evaluated. Box plots show the variation in the number of points per cylinder for different cylinder diameters, point triggering models, and laser beam diameters at exit from the scanner. The red dots indicate the median number of points after filtering the point cloud (points must be closer than 10% of the cylinder diameter, and, if not, then closer than 2 cm). The point triggering model "geometric" simulates a laser scanner with an infinitesimally small laser beam.

do not match reality exactly. Prefiltering effects are assumed to be reproduced in a realistic way and surely provide realistic implications. The primary objective of the simulation study was not to reproduce exactly the same scanning results of the three devices investigated, but to allow general conclusions to be made regarding the effects of different signal triggering approaches. Nevertheless, the effect of the laser beam size is based on realistic assumptions, as the effect of its size is precisely reproducible.

There are various effects that could additionally be considered with the simulation approach used in this study, such as
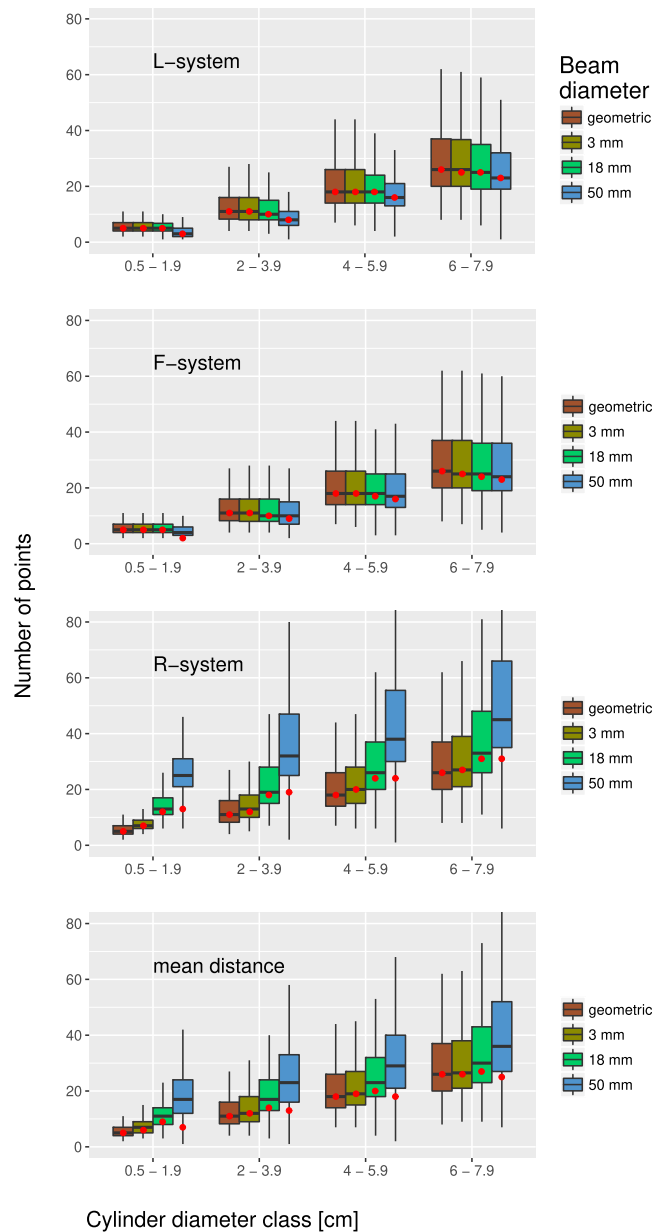
the intensity of the reflected light, multiple reflectance of the photons of the laser pulse, the influence of incidence angles on the objectives, and errors in the range measurement of the different devices.

An important finding of the present study for forest inventory applications is that small objects lack appropriate representation in point clouds of the signal triggering approaches investigated here, in which points are either prefiltered or subject to a deviation from the object's surface. Information on small objects deteriorates even more with increasing distance

to the scanner, especially in environments with a high density of objects, due to occlusion and an increasing probability of mixed pixel situations. This implies that scanning small branches (e.g., less than 2 cm in diameter) in tree crowns (large distance to the scanner) with many small branches (high density) will be nearly impossible when tree crown reconstruction is the objective of the application. In such a situation, scanners with small laser beam diameters perform slightly better. On the other hand, larger laser beam diameters, in combination with multiple triggering, deliver more points per object. Larger branch diameters (e.g., up to 6 cm) are also difficult to represent, depending on the application. Another problem occurring with large laser beam diameters is that the object shape tends to be flattened. This could lead to a bias in diameter estimation, e.g., when applying the widely used Hough transform approach (see [33]–[36]) to fit circles or cylinders in the point cloud.

These findings indicate that TLS-based wood volume estimations of smaller trees might be severely impacted, as well as estimations of small branches. Depending on the triggering approach, small branches are either underestimated, because of prefiltering and occlusion, or overestimated, through the distance deviation of points. Scanning in dense forests, e.g., those with understorey, will increase occlusion effects considerably (see [21]), further reducing the number of visible objects. In addition, we expect additional noise in the point clouds due to an increment in mixed pixel effects caused by laser pulses intersecting with multiple small branches. Similar effects are to be expected when scanning during the growing season (leaf-on conditions), when additional problems of separating echoes from leaves and woody parts would arise. In addition to these technical limitations, even slight wind or precipitation would add further noise to the point cloud. Nevertheless, we expect that TLS-based wood volume estimations of large trees or large branches are mostly accurate since the ratio of erroneous points is decreasing with increasing object size. Therefore, if diameter thresholds are chosen appropriately, TLS is still the most promising approach for tree volume estimation. Yet, future simulation experiments, including volume estimation approaches, need to be conducted to examine details of volume estimation.

V. CONCLUSION

In this study, we investigated the edge noise effects of three terrestrial laser scanners. We used their scanning properties to evaluate the influence of signal triggering approaches, laser beam diameters, and stand properties on the quality of the point cloud. We show that these devices handle ambiguous signals from a controlled experiment, with obstacles placed in the laser beam, with different approaches: prefiltering, multiple-signal triggering, and deviation of points from object surfaces. All approaches have disadvantages, either leading to a lack of information or biased information. In a simulation study with 684 stand diameter distributions, we show that especially, small objects (twigs and small branches) in combination with large (or strongly diverging) laser beams produce lower point cloud quality. These effects are increased when objects are farther away from the scanner and/or the density of objects is

high, for example, in tree crowns. We, therefore, recommend the choice of a targeted branch diameter to be measured of at least 2 cm, whereas a reasonable diameter would be the one for "merchantable" wood ($\geq$7 cm), which is widely used in NFI reporting. Furthermore, we recommend using terrestrial laser scanners with a small footprint if object reconstruction is intended. If the gap probability of a stand needs to be assessed, a device with multiple-signal triggering will provide more information with a similar angular resolution than devices with single-signal triggering. These findings contribute to the ability to set realistic objectives when applying TLS for forest inventories and support the selection of suitable scanners.

REFERENCES

[1] *The State of the World's Forests 2018. Forest Pathways to Sustainable Development*, Food Agricult. Org. United Nations (FAO), Rome, Italy, 2018.
[2] A. Shvidenko, C. V. Barber, and R. Persson, *Forest and Woodland Systems*. Washington, DC, USA: Island Press, 2005, ch. 21, pp. 585–621. [Online]. Available: http://www.millenniumassessment.org/documents/document.290.aspx.pdf
[3] Y. Pan *et al.*, "A large and persistent carbon sink in the world's forests," *Science*, vol. 333, pp. 988–993, Aug. 2011.
[4] L. Waser, C. Ginzler, and N. Rehush, "Wall-to-wall tree type mapping from countrywide airborne remote sensing surveys," *Remote Sens.*, vol. 9, no. 8, p. 766, Jul. 2017, doi: 10.3390/rs9080766.
[5] X. Liang *et al.*, "Terrestrial laser scanning in forest inventories," *ISPRS J. Photogramm. Remote Sens.*, vol. 115, pp. 63–77, May 2016
[6] F. Morsdorf, D. Kükenbrink, F. D. Schneider, M. Abegg, and M. E. Schaepman, "Close-range laser scanning in forests: Towards physically based semantics across scales," *Interface Focus*, vol. 8, no. 2, Apr. 2018, Art. no. 20170046.
[7] J. L. Lovell, D. L. B. Jupp, G. J. Newnham, N. C. Coops, and D. S. Culvenor, "Simulation study for finding optimal lidar acquisition parameters for forest height retrieval," *Forest Ecol. Manage.*, vol. 214, nos. 1–3, pp. 398–412, Aug. 2005.
[8] M. Disney, P. Lewis, and P. Raumonen, "Testing a new vegetation structure retrieval algorithm from terrestrial lidar scanner data using 3D models," in *Proc. Silvilaser*, Vancouver, BC Canada, Sep. 2012, pp. 1–9.
[9] D. Van der Zande, I. Jonckheere, J. Stuckens, W. W. Verstraeten, and P. Coppin, "Sampling design of ground-based lidar measurements of forest canopy structure and its effect on shadowing," *Can. J. Remote Sens.*, vol. 34, no. 6, pp. 526–538, 2008.
[10] J. Binney and G. S. Sukhatme, "3D tree reconstruction from laser range data," in *Proc. IEEE Int. Conf. Robot. Autom.*, Kobe, Japan, May 2009, pp. 1321–1326.
[11] A. Hovi and I. Korpela, "Real and simulated waveform-recording LiDAR data in juvenile boreal forest vegetation," *Remote Sens. Environ.*, vol. 140, pp. 665–678, Jan. 2014, doi: 10.1016/j.rse.2013.10.003.
[12] A. Kukko and J. Hyyppä, "Laser scanner simulator for system analysis and algorithm development: A case for forest measurements," in *Proc. Laser Scanning SilviLaser*, 2007, pp. 234–240.
[13] M. D. Adams and P. J. Probert, "The interpretation of phase and intensity data from AMCW light detection sensors for reliable ranging," *Int. J. Robot. Res.*, vol. 15, no. 5, pp. 441–458, Oct. 1996.
[14] G. Newnham *et al.*, "Evaluation of terrestrial laser scanner for measuring vegetation structure," in *Proc. CSIRO Sustain. Agricult. Flagship*, 2012, pp. 1–32, 2012. [Online]. Available: https://publications.csiro.au/rpr/download?pid=csiro:EP124571&dsid=DS3
[15] W. Wagner, A. Ullrich, T. Melzer, C. Briese, and K. Kraus, "From single-pulse to full-waveform airborne laser scanners: Potential and practical challenges," in *Proc. ISPRS 20th Congr.*, vol. 35, 2004, pp. 1–6. [Online]. Available: http://www.isprs.org/proceedings/XXXV/congress/comm3/papers/267.pdf

[16] B. Jutzi and U. Stilla, "Measuring and processing the waveform of laser pulses," *Opt. 3-D Meas. Techn. VII*, vol. 1, pp. 194–203, 2005.

[17] M. Disney, V. Kalogirou, P. Lewis, A. Prieto-Blanco, S. Hancock, and M. Pfeifer, "Simulating the impact of discrete-return lidar system and survey characteristics over young conifer and broadleaf forests," *Remote Sens. Environ.*, vol. 114, no. 7, pp. 1546–1560, 2010.

[18] S. Kaasalainen *et al.*, "Brightness measurements and calibration with airborne and terrestrial laser scanners," *IEEE Trans. Geosci. Remote Sens.*, vol. 46, no. 2, pp. 528–534, Feb. 2008.

[19] K. Koenig *et al.*, "Radiometric correction of terrestrial LiDAR data for mapping of harvest residues density," *ISPRS Ann. Photogramm., Remote Sens. Spatial Inf. Sci.*, vols. II–5/W2, pp. 133–138, Oct. 2013.

[20] Blender Online Community and Blender Institute, Amsterdam. (2015). *Blender—A 3D Modelling Rendering Package*. [Online]. Available: http://www.blender.org

[21] M. Abegg, D. Kükenbrink, J. Zell, M. E. Schaepman, and F. Morsdorf, "Terrestrial laser scanning for forest inventories—Tree diameter distribution and scanner location impact on occlusion," *Forests*, vol. 8, no. 184, pp. 1–29, 2017.

[22] M. Gschwandtner, R. Kwitt, A. Uhl, and W. Pre, "Blensor: Blender sensor simulation toolbox," in *Advances in Visual Computing*, vol. 6939, G. Bebis *et al.*, Eds. Las Vegas, NV, USA: Springer-Verlag, 2011, pp. 199–208.

[23] I. Szwarcbaum and G. Shaviv, "A Monte-Carlo model for the radiation field in plant canopies," *Agricult. Meteorol.*, vol. 17, no. 5, pp. 333–352, 1976, doi: 10.1016/0002-1571(76)90087-X.

[24] Y. M. Govaerts and M. M. Verstraete, "Raytran: A Monte Carlo ray-tracing model to compute light scattering in three-dimensional heterogeneous media," *IEEE Trans. Geosci. Remote Sens.*, vol. 36, no. 2, pp. 493–505, Mar. 1998.

[25] P. Lewis, "Three-dimensional plant modelling for remote sensing simulation studies using the botanical plant modelling system," *Agronomie*, vol. 19, nos. 3–4, pp. 185–210, 1999.

[26] *Leica BLK360 Imaging Scanner. 3D Reality. Now*, Leica Geosyst. AG, Heerbrugg, Switzerland, 2017.

[27] *FARO Laser Scanner Focus 3D*, FARO Technol. Inc., Lake Mary, FL, USA, 2013.

[28] *Data Sheet, RIEGL VZ-1000*, Riegl Laser Meas. Syst. GmbH, Horn, Austria, Mar. 2015.

[29] D. Mandallaz, *Sampling Techniques for Forest Inventories* (Chapman & Hall/CRC Applied Environmental Statistics). Boca Raton, FL, USA: Chapman & Hall, 2006.

[30] R Core Team, "R: A language and environment for statistical computing," R Found. Stat. Comput., Vienna, Austria, Tech. Rep., 2017. [Online]. Available: https://www.R-project.org/

[31] H.-G. Maas and G. Vosselman, Eds., *Airborne and Terrestrial Laser Scanning*. Boca Raton, FL, USA: CRC Press, 2010.

[32] C. Mallet and F. Bretar, "Full-waveform topographic lidar: State-of-the-art," *ISPRS J. Photogramm. Remote Sens.*, vol. 64, no. 1, pp. 1–16, Jan. 2009.

[33] M. Simonse, T. Aschoff, H. Spiecker, and M. Thies, "Automatic determination of forest inventory parameters using terrestrial laser scanning," in *Proc. ScandLaser Sci. Workshop Airborne Laser Scanning Forests*, Umeå, Sweden, Sep. 2003, pp. 251–257. [Online]. Available: http://pub.epsilon.slu.se/9060/1/hyyppa_et_al_120814.pdf

[34] P. V. C. Hough, "Method and means for recognizing complex patterns," U.S. Patent 3 069 654, Dec. 18, 1962.

[35] A. Bienert, S. Scheller, E. Keane, F. Mohan, and C. Nugent, "Tree detection and diameter estimations by analysis of forest terrestrial laserscanner point clouds," in *Proc. ISPRS Workshop Laser Scanning SilviLaser*, vol. 36, Sep. 2007, pp. 50–55.

[36] J. Heinzel and M. Huber, "Tree stem diameter estimation from volumetric TLS image data," *Remote Sens.*, vol. 9, no. 6, p. 614, Jun. 2017.

Meinrad Abegg received the M.Sc. degree in forest sciences from ETH Zurich, Zürich, Switzerland, in 2003 and the Ph.D. degree in geography from the University of Zurich (UZH), Zürich, in 2020. Since 2004, he has been employed by the Swiss National Forest Inventory (NFI), Swiss Federal Institute for Forest, Snow and Landscape Research (WSL), Birmensdorf, Switzerland, working on different subjects along the workflow from field measurements to outreach products with NFI results. His research interests include the application of terrestrial laser scanning (TLS) for forest inventories, inventory statistics, NFI data processing, and development of field methods for forest inventories.

Ruedi Boesch received the Ph.D. degree in geography from the University of Zurich, Zürich, Switzerland, in 1992.

Since 1992, he has been employed by the Swiss Federal Institute for Forest, Snow and Landscape Research, Birmensdorf, Switzerland, as a Scientific Researcher. His research interests include remote sensing, animal speech processing, and image analysis methods.

Michael E. Schaepman (Senior Member, IEEE) received the M.Sc. and Ph.D. degrees in geography from the University of Zurich (UZH), Zürich, Switzerland, in 1993 and 1998, respectively.

In 1999, he was a Post-Doctoral Researcher with the Optical Sciences Center, University of Arizona, Tucson, AZ, USA. In 2000, he was appointed as the Project Manager of the APEX Spectrometer, European Space Agency, Paris, France. In 2003, he became the Full Chair of geoinformation science and remote sensing at Wageningen University, Wageningen, The Netherlands. In 2009, he was appointed as the Full Chair of remote sensing at UZH, where he has been the Head of Remote Sensing Laboratories, Department of Geography. He also has been the Director of the University Research Priority Program on Global Change and Biodiversity and the Vice President of research. Since 2020, he is the President of the UZH. His research interests include computational Earth sciences using remote sensing and physical models, with a particular focus on the land–atmosphere interface using imaging spectroscopy.

Felix Morsdorf received the M.Sc. degree in physical oceanography from the University of Kiel, Kiel, Germany, in 2001, and the Ph.D. degree in geography, with a specialization in LIDAR remote sensing, from the University of Zurich, Zürich, Switzerland, in 2007.

He is the Group Leader with the Department of Geography, University of Zurich. His group uses empirical and physical approaches to bridge the semantic gap between data and information. His research is focused on laser scanning and vegetation structure.